Vortex Characteristics Analysed from HART Data

Berend G. van der Wall
DLR, Institute for Flight Mechanics
Braunschweig, Germany

Abstract

This paper analyses the detailed data taken during the HART test 1994 on a pressure instrumented BO105 hingeless model rotor. Leading edge pressure distribution provides information, over which part of the rotor disk vortices passed on top, where they penetrate the disk and where they are below. The intensity of BVI is qualitatively visible. From pressure distribution along chord in the outer part of the blade, the load distribution and therewith the blade bound circulation can be computed. This results into the strength, sense of rotation, the number and the radial position of tip vortices trailed into the wake. Flow visualisation by LLS technique provides the vortex trajectories in space at a desired blade azimuth and the vortex passage height and time through the LDV measurement range, and its inclination angles with respect to the LDV position, can be derived from these data. 3D velocity vectors within a wide time window are available by LDV measurements along two vertical lines. These data provide information about the vortex structure, i.e. vorticity distribution, vector field, core radius, circulation, height and time of passage of the vortex center through the LDV measurement range. All of these data are used in this paper to analyse the vortex structures, to compare LLS and LDV results where possible and to point on non-compatibilities found between the results.

Nomenclature

Abbreviations

BL	Baseline
BVI	Blade Vortex Interaction
DNW	German-Dutch Windtunnel
HART	HHC Aeroacoustic Rotor Test
HHC	Higher Harmonic Control
LDV	Laser Doppler Velocimetry
LLS	Laser Light Sheet
MN	Minimum Noise
MV	Minimum Vibration
PIV	Particle Image Velocimetry

Symbols

c	airfoil chord, $0.121m$
C_T	thrust coefficient
L	lift, N
M	Mach number
r	radial coordinate, m
R	rotor radius, $2m$
t	time, s
$u,\ v,\ w$	velocity components, m/s
V	velocity, m/s
$x,\ y,\ z$	coordinates, m
α	angle of attack, rad
β	LDV-vortex interaction angle, rad
Γ	circulation, m^2/s
μ	advance ratio
ρ	air density, kg/m^3
ϕ	angle around vortex axis, rad
$\psi = \Omega t$	azimuth (nondim. time), rad
ω	vorticity, $1/s$
Ω	rotor rotational speed, $109rad/s$

Indices

0	vortex center passing the LDV position
av	average value
$b,\ t,\ s$	bound to the blade, trailed, shed
c	vortex core
eq	equivalent
S	shaft
tip	at blade tip
$x,\ y,\ z$	w.r.t. coordinates
V	vortex

Introduction

HHC was known to be an effective device to successfully reduce rotor BVI noise [1], but its functionalism was widely unknown. In 1994 the HART test [2] was conducted in the DNW with 22 days of testing, aiming to understand this functionalism of HHC on BVI noise emission [4]. For this purpose, an existing 4-bladed Mach-scaled hingeless BO105 model rotor (40% scale of the original), equipped with numerous pressure transducers and strain gauges for blade loading and blade motion analysis was used, [5, 6]; a microphone array traversed to measure the noise emission in a plane below the rotor [7], an LLS equipment was used to locate the tip vortices before and after the interaction with a blade [8], and two LDV systems simultaneously measured flow components along two different vertical lines within the rotor disk for vortex analysis purposes [9, 10, 11, 12]. This huge experimental setup was possible only due to combined efforts of an international prediction and test team, comprising DLR, ONERA, DNW, NASA and US Army AFDD. Numerous publications exist about efforts have been

$\alpha_S/^o$	μ	M_{tip}	C_T
5.3	0.152	0.638	0.0043

Table 1: Rotor operational conditions for cases BL, MN, and MV. The hub moments are trimmed to zero.

made prior to the test [13, 14, 15, 16], about the test [17, 18, 19, 20] and in the aftermath for code validation [21, 22, 23, 24, 25, 26, 27, 28].

The rotor operational condition is given in Tab. 1, and 3 cases of interest are investigated here. First, the baseline case (BL) does not incorporate any HHC and is representative for a 6.5^o descent flight. Second, the minimun noise HHC setting (MN) incorporates $3/rev$ HHC with an amplitude of 0.86^o and a phase of 300^o for minimizing the average noise level measured in a plane below the rotor. Third, the minimum vibration HHC setting (MV) using the same control frequency and amplitude, but with a different phase angle of 180^o. The rotor blade is preconed by 2.5^o, twisted by $-8^o/R$ and has a modified NACA 23012 airfoil. A detailed description of the blade dynamics properties, sensor characteristics, test setup and test matrix, data acquisition, and representative test results are presented in [4].

In the HART related publications, the LDV data were taken as published in [4], i.e. in the experimental coordinate system parallel to the wind tunnel flow, since the LDV systems directed normal to the mean flow. The LDV measurement ranged along a vertical line at constant longitudinal and lateral position as described in Tab. 2. The vortex axis inclination to the LDV data plane was not taken into account.

In the following, sections, first the blade bound circulation will be analysed from pressure distribution data to obtain the initial vortex strength and spanwise location. From LLS data the vortex axis inclination with respect to the LDV measurement is extracted and with this information the LDV data are transformed into a plane virtually normal to the vortex axis. In this plane, vortex properties will be analysed, i.e. vorticity, center of the vortex, core radius, circulation, and axial velocity.

Blade circulation

Sectional pressure distribution

At three radial sections, i.e. $r/R = 0.75$, 0.87 and 0.97 the unsteady pressure has been measured along chord to obtain the sectional lift dL/dr via chordwise numerical integration. Defect sensors within the distribution are numerically replaced by linear interpolation of the neighbouring sensor signals. Due to the high density of instrumentation, namely 24 transducers at $r/R = 0.87$, and 44 at each of the other sections, this is not significantly affecting the integrated values.

Blade bound circulation

From simple quasisteady theory, the blade bound circulation may be obtained from the sectional

Side:	advancing		
Case:	BL	MN	MV
x_{LDV}/R	0.443	0.448	0.448
y_{LDV}/R	0.605	0.601	0.601
	-0.0818	-0.1285	-0.0634
z_{LDV}/R	⋮	⋮	⋮
	0.0202	-0.0085	0.0566
Side:	retreating		
Case:	BL	MN	MV
x_{LDV}/R	0.376	0.376	0.376
y_{LDV}/R	-0.706	-0.706	-0.706
	-0.121	-0.1175	-0.105
z_{LDV}/R	⋮	⋮	⋮
	0.011	0.035	0.045

Table 2: LDV locations in the hub fixed wind tunnel coordinate system.

lift by $\Gamma_b = (dL/dr)/\rho V$, with the lift computed as noted above. The local velocity is taken as $V = \Omega R(r/R + \mu \sin\psi)$, and ρ results from the wind tunnel data. At the interesting azimuthal positions of $\psi_t \approx 143^o$ and 225^o, where the vortices measured later on by the LDV systems are created, the radial bound circulation distribution provides information of what the initial vortex strength must have been. In Fig. 1 the low pass filtered radial bound circulation distribution is shown for the three cases BL, MN and MV at both of the azimuthal positions. It can be seen that on the retreating side the differences between the three cases is not large, while on the advancing side the radial distribution changes dramatically due to HHC and is even negative close to the tip in the MV case. This is known to create a counterrotating double vortex system with a tip vortex of opposite sense of rotation and an inboard positioned vortex of normal rotation. Due to the small gradient $d\Gamma_b/dr$ at the tip in the BL case (advancing side), the vortex will be created at an inboard station.

Circulation trailed into the wake

Using the methodology of analysing the bound circulation distribution as described in [27, 29] for the vortex roll-up process, the amount of circulation fed into the rolled-up vortex can be computed. This normalization may be interpreted either by comparing an equivalent circulation at a constant oncoming velocity along span [27] or to a constant way traveled by the section of interest [29].

$$\Gamma_{b,eq} = \Gamma_b V/V_{tip} = \Gamma_b \frac{r/R + \mu\sin\psi}{1 + \mu\sin\psi} \qquad (1)$$

The equivalent circulation $\Gamma_{b,eq}$ defines the radial extension of vorticity trailed into the tip vortex Δr_b, and the geometrical center of the derivative $d\Gamma_{b,eq}/dr$ marks the radial position of the rolled-up vortex, r_t. The peak-to-peak difference of the equivalent circulation, $\Delta\Gamma_{b,eq}$,

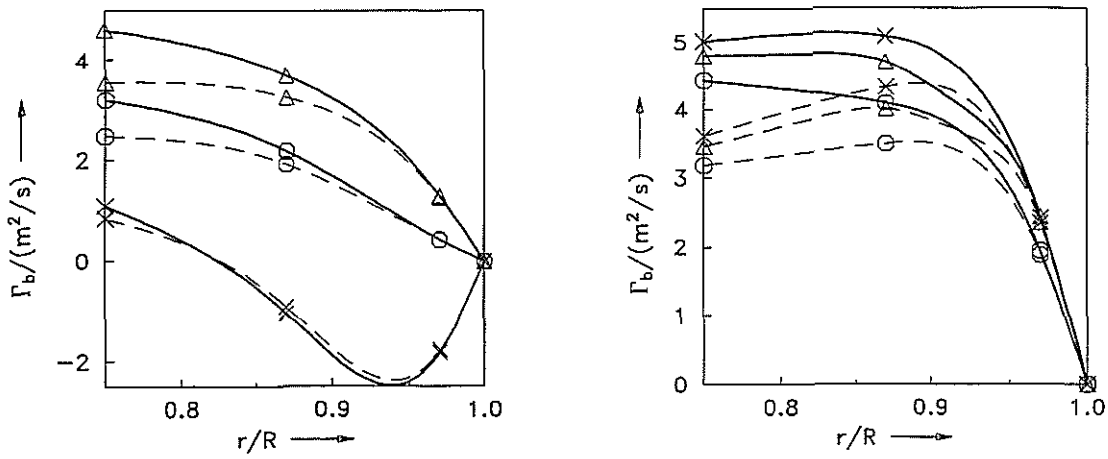

(a) $\psi_t = 143^o$ (b) $\psi_t = 225^o$

Figure 1: Radial distribution of bound circulation for BL (○), MN (△) and MV (×). ——: Γ_b, - - - -: $\Gamma_{b,eq}$.

Side:	advancing				retreating		
Case:	BL	MN	MV	MV (u)	BL	MN	MV
$\Gamma_V/(m^2/s)$	2.65	3.76	3.73	-2.44	3.67	4.18	4.58
r_t/R	0.916	0.932	0.866	0.980	0.964	0.959	0.965
$\Delta r_b/R$	0.25	0.2	0.225	0.060	0.110	0.125	0.105

Table 3: Circulation trailed into the tip vortices from Eq. 2, radial tip vortex location, and radial extension of vorticity trailed into a vortex. (u) denotes the upper vortex.

builds the normalized strength, and the inverse normalization of Eq. 1 at the final radial position defines the circulation finally trailed into the vortex.

$$\Gamma_V = \Delta\Gamma_{b,eq}\frac{1+\mu\sin\psi}{r_t/R+\mu\sin\psi_t} \qquad (2)$$

The values, deduced from Fig. 1, are listed in Tab. 3. Since the normalization procedure shifts the maximum of the bound circulation more to the tip and defines the radial extension of circulation fed into one vortex, the resulting vortex circlulation is little less than what could be directly read from Fig. 1. It shall also be noted, that the equivalent circulation exhibits a maximum, where the original circulation distribution still shows a gradient.

BVI events

From the leading edge pressure distribution, BVI events in the rotor disk are identified easily, when the first 6 integer harmonics of the pressure data are omitted. This high pass filtering leaves all vortex induced fluctuations in the data but suppresses the $1/rev$ dynamic pressure fluctuations and the basic components due to blade motion of the lower elastic modes. By this, the number and, qualitatively, the closeness of interaction with a blade can be analysed. For this study it is important how often and how close the vortex segments measured later on by LDV have interacted with a blade, since a close interaction will disturb the vortex core to a certain amount. In Fig. 2 these filtered pressure data are presented and the assumed flight paths from the points of creation at the front of the rotor disk to the LDV measurement locations are indicated. Along these flight paths, the BL case shows one close interaction just before the LDV position is reached on the advancing side; the vortex is above the rotor blade at this interaction. On the retreating side, there is also one close interaction just upstream the LDV measurement location, and the vortex is again above the blade.

In the MN case, there is a very close encounter at $\psi \approx 90^o$ on the advancing side, and the vortex is below the blade at the LDV location. On the retreating side, just upstream of the LDV position, the vortex seems to be cut by a rotor blade, since along the vortex flight path this is the strongest interaction. The remnants of this event shall be visible in the LDV data presented in a later section. The MV case appears to have no close interaction of a vortex between its creation and the appropriate LDV position on neither the advancing nor the retreating side. All close BVI events happen downstream of the LDV location, i.e. the vortices are flying higher over the rotor disk before penetrating it, compared to BL and MN cases. Thus, both of the vortices shall be clearly visible in the LDV data.

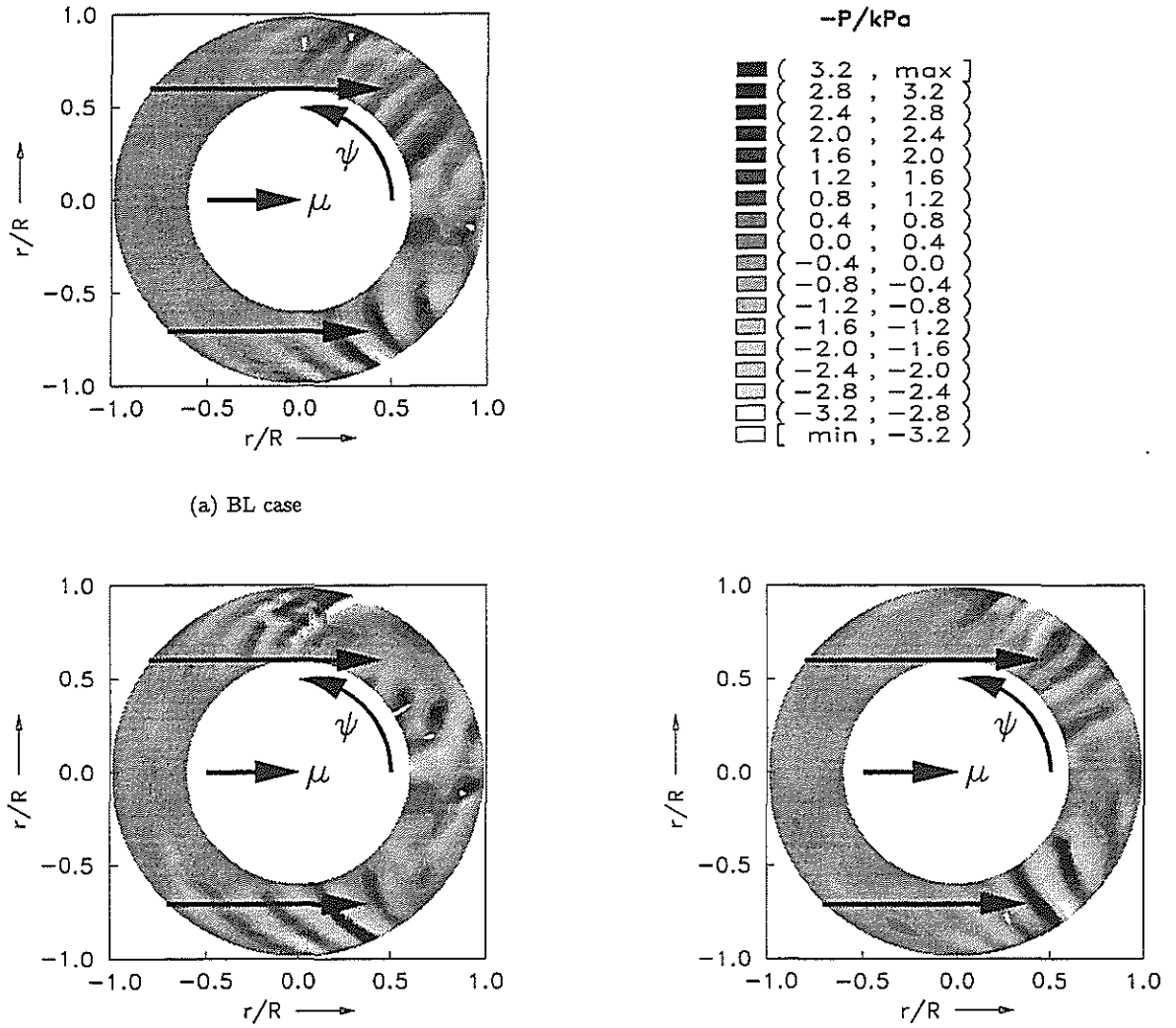

(a) BL case

(b) MN case

(c) MV case

Figure 2: Pressure distribution (time averaged data) at 3% chord, upper side. Data are high pass filtered at 6/rev to show vortex induced fluctuations only. The LDV measurement positions are located at the end of the arrowheads that indicate the flight path of the vortices created at $\psi = 143°$ and $\psi = 225°$.

Vortex trajectories

LLS data

At a blade position of $\psi = 35°$ on the advancing side and $\psi = 295°$ on the retreating side the vortex center positions in space were computed from LLS recordings [30]. For each vortex, different lateral positions are captured and thus the vortex axis orientation in space can be evaluated. This is done for the tip vortices of two different consecutive blades such that two vortex trajectories are visible. Assuming each vortex to move the same way, the flight path may be approximated to vary almost linearly between the x, z coordinates at a constant lateral position. Since these data are obtained close to the LDV measurement location oriented vertical in space, the analysis of LLS data is important for transforming the LDV data from the wind tunnel coordinate system into the vortex axis system. It must be noted, that all vortex trajectories from the HART test published before [4] were based on the analysis of a single LLS recording only. Thus, each vortex point is a result from a different revolution, but at the same reference blade azimuth. For this paper, all of the trajectories have been recompiled from as many single recordings as available in order to evaluate time averaged vortex data. The resulting trajectories are much smoother than those of the single recording analysis in cases MN and MV on the advancing side, but do not change in the rest of the cases.

Vortex axis orientation

The results from LLS data analysis is given in Fig. 3 for the advancing side of the rotor and in Fig. 4 for the retreating side, all in the wind tunnel coordinate system with the origin in the center of the rotor

hub. Additionally, the LDV measurement range is indicated in the figures and the probable height of vortex passage through the LDV measurement line can be extracted. In all cases the vortices pass the LDV range and shall be visible in the LDV data. On the advancing side, Fig. 3, the trajectories do change significantly between the three cases. In the BL case, the vortices are almost parallel to the blade (b) and are in the same height, this being the reason for the high BVI noise level. In the MN case, the vortices are far below the blade at the tip, but inboard they have a steep gradient towards the blade. This is in agreement with the pressure data of Fig. 2(b), that indicate the penetration of the rotor disk to be at $y/R \approx 0.4$. The MV case also has a strong inclination of the vortex axis with respect to the blade axis, but is very close to the blade at the tip, where the largest Mach numbers are present. Therefore, this case is noisier than the BL case [4].

The results of the retreating side are given in Fig. 4. From the top view, all cases do look similar, but the rear view shows differences in closeness to the blade as well as in the inclination angles. Due to the shaft angle setting, the blade will move downwards when it reaches the vortex 5. Thus, case MV (f) is more problematic with respect to noise than case BL (b), since the vortex is closer to the blade and has less inclination in radial direction.

From these figures the intersection angles between the vortex axis and the LDV measurement line can be extracted. In the top view, the angle between the projected vortex axis and a plane $z = const.$ will be denoted as β_z, and in the rear view, the appropriate angle to a plane $x = const.$ will be taken as β_x. These angles are important later on for transforming the LDV data, since the vortex passed the LDV measurement line with those angles of inclination. They are given in Tab. 4, and it is obvious, that they are large enough such that vortex properties as vorticity, circulation or core radius cannot be evaluated from the data in the wind tunnel coordinate system as was done in [4, 31, 12]. From Fig. 3 and Fig. 4 the vertical position z_0 of the vortex passage through the LDV measurement range and the time of passage in terms of rotor azimut, ψ_0, can be evaluated. Both values are also listed in Tab. 4 for all cases.

Velocity vector field analysis

The velocity vector fields on advancing and retreating side published up to today [4, 31, 12] were presented in the wind tunnel coordinate system, i.e. with velocity components u, w in a plane $y = const.$ and v normal to it. Therein the x-coordinate was build up by the average horizontal flow component within the assumed vortex center, $x = x_{LDV} - u_{av}(t - t_0)$, and the z-coordinate is equivalent to the vertical LDV position plus the average vertical flow component within the vortex center, $z = z_{LDV} - w_{av}(t - t_0)$. It was implicitly assumed, that the mean flow would not change within this virtual x, z-range, but this is quite questionable in a highly three-dimensional rotor flow environment. The only reliable coordinates are the LDV measurement positions, the measurement time window (or the equivalent in rotor azimuth), and the wind tunnel speed (or the advance ratio). In the following, the virtual x-coordinate is build up by these variables: $x/R = x_{LDV}/R - \mu\psi$, and $z = z_{LDV}$. x_{LDV} and z_{LDV} are the LDV measurement coordinates in the hub fixed wind tunnel coordinate system.

Transformation into the vortex axis

In the section above, the intersection angles between the vortex axis and the LDV measurement line were identified. To obtain the measured velocities in the vortex axis system, both the x, z coordinates and the velocities have to be transformed by these angles. x_0 and z_0 define the vortex center in the wind tunnel system.

$$\begin{aligned} x_V &= (x - x_0)\cos\beta_z \\ z_V &= (z - z_0)\cos\beta_x \\ u_V &= u\cos\beta_z - v\sin\beta_z \\ v_V &= (u\sin\beta_z + v\cos\beta_z)\cos\beta_x - w\sin\beta_x \\ w_V &= (u\sin\beta_z + v\cos\beta_z)\sin\beta_x + w\cos\beta_x \end{aligned} \tag{3}$$

Then the average values of the transformed velocity field are subtracted in order to mainly show the vortex induced velocities. Unfortunately, in most of the measurement areas the wake of one or two blades that had passed the measurement line just before do significantly affect the average values. Therefore, the area of analysis must carefully be selected to keep these zones outside the area of investigation. For the vector field analysis, the assumption is made that the velocity field in a plane normal to the vortex axis does not change within the axial range where the LDV data are taken. Therefore, all data are shifted into a plane $y_V = const.$. Since the vortex is fed with a continuously varying circulation, and is within a highly three-dimensional flow field, this is basically questionable. However, the small ranges around the center of a vortex are within a small volume and the $3/rev$ changes of vortex circulation due to HHC within this small volume may be negligible, because they do have a large wavelength compared to the range of interest.

Vorticity and vortex circulation

Within the velocity vector field obtained from Eq. 3, the vorticity can be examined by

$$\omega_y = \frac{rot(V_V)}{2} = \frac{\partial u_V/\partial z_V - \partial w_V/\partial x_V}{2} \tag{4}$$

and the circulation of the field is computed by integrating the positive values of vorticity for a vortex of conventional sense of rotation, or by the negative values for a counterrotating vortex (as is present in the

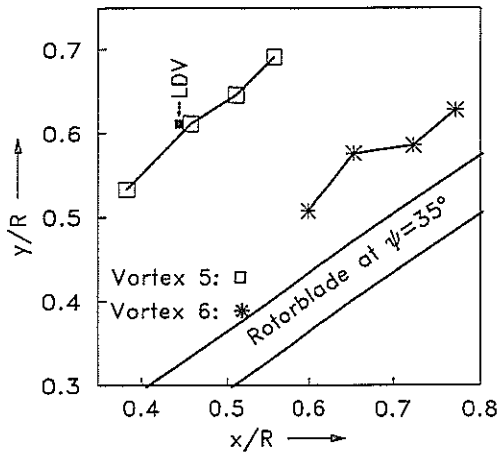

(a) BL case, top view

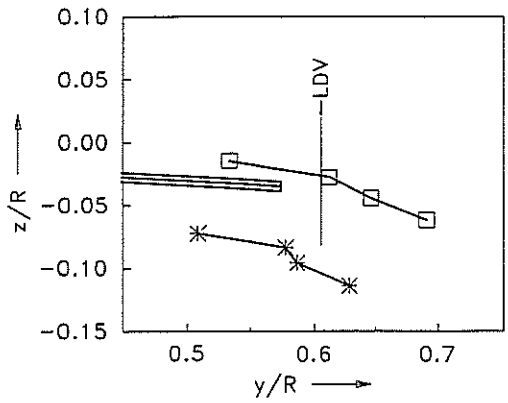

(b) BL case, rear view

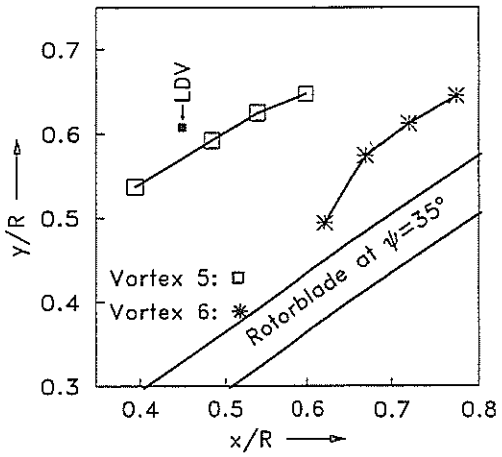

(c) MN case, top view

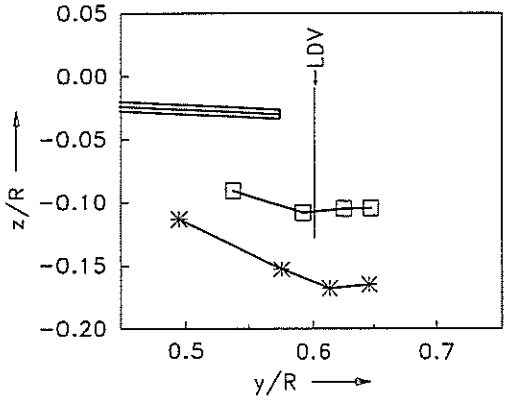

(d) MN case, rear view

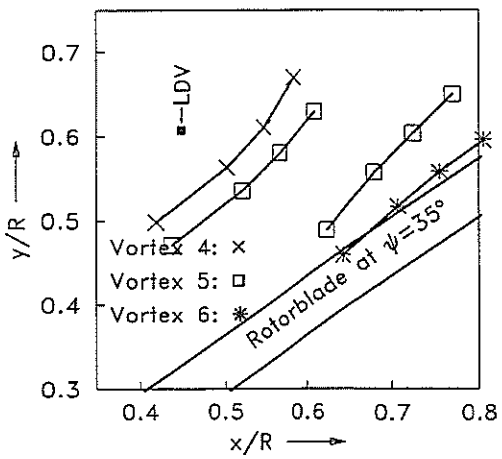

(e) MV case, top view

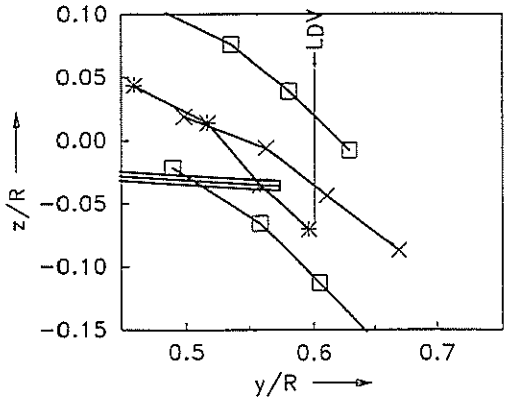

(f) MV case, rear view

Figure 3: Vortex trajectories at $\psi = 35°$ on the advancing side. In (a), (c), (e) the wind tunnel flow comes from the left.

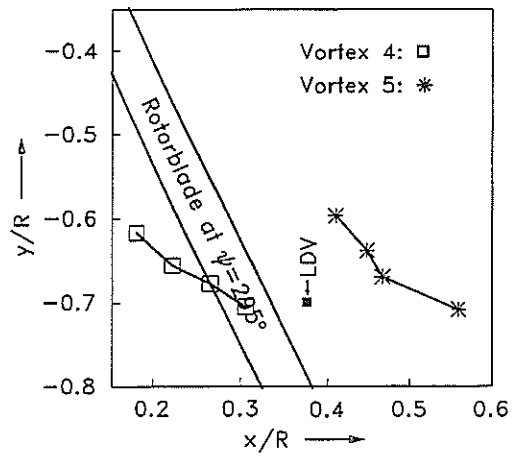

(a) BL case, top view

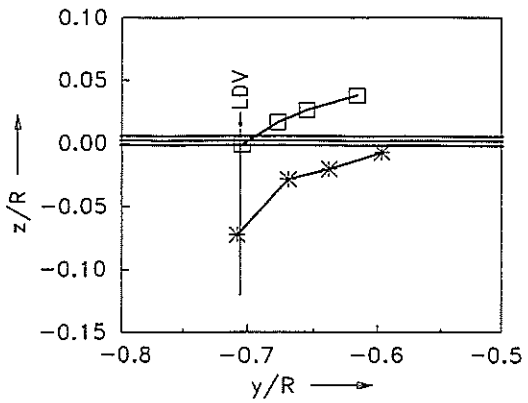

(b) BL case, rear view

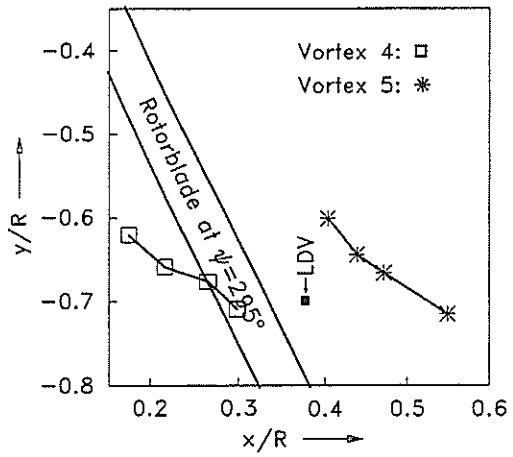

(c) MN case, top view

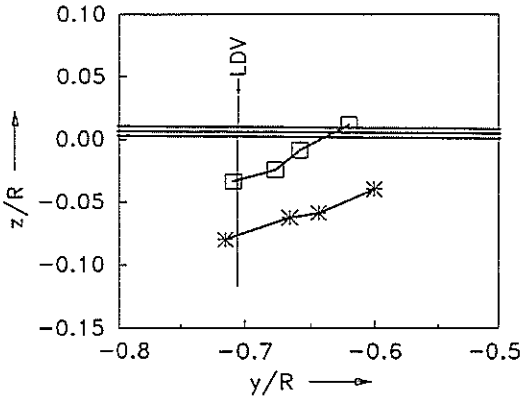

(d) MN case, rear view

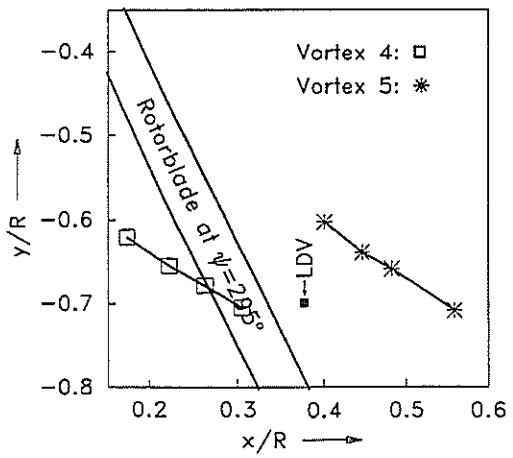

(e) MV case, top view

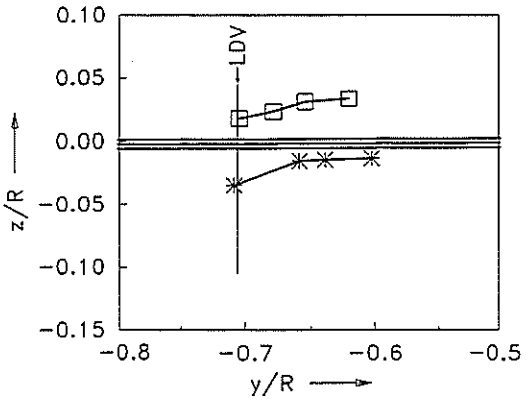

(f) MV case, rear view

Figure 4: Vortex trajectories at $\psi = 295^o$ on the retreating side. In (a), (c), (e) the wind tunnel flow comes from the left.

Side:	advancing				retreating		
Case:	BL	MN	MV	MV (u)	BL	MN	MV
$\beta_z/^o$	49	60	44	42	-57	-57	-58
$\beta_x/^o$	16	-5	38	42	-34	-17	-17
$100z_0/R$	-2.3	-7.8	0.4	6.0	-1.8	-4.0	0.0
$\psi_0/^o$	30	10	352	340	326	329	324

Table 4: Vortex inclination angles and height of passage through the LDV measurement range. (u) denotes the upper vortex.

MV case).

$$\Gamma = 2\int\int \omega_y \, dx \, dz = 2\int_0^{2\pi}\int \omega_y \, dr \, r \, d\phi \qquad (5)$$

This areal integration is done numerically using the first expression. The second expression of Eq. 5 may be simplified when an ideal vortex is assumed, since the angular integral around the vortex axis ϕ can be solved in advance and the remaining integral is the circumferential velocity, V_ϕ. Thus,

$$\Gamma = 2\pi r V_\phi \qquad (6)$$

At $\phi = 0, r = x_V$ and $V_\phi = w_V$ and this can be used for computing the vortex circulation as well, if the vortex is ideal in its vorticity distribution. An alternative is using the u_V-profile versus z_V, a result at $\phi = 90°$, where $r = z_V$ and $V_\phi = u_V$. Eq. 6 is used in [31] in the wind tunnel coordinate system, but it is obvious, that the measured vorticity does not fulfill the requirement of an ideal vortex on the advancing side, see Fig. 5.

A different approach was used by ONERA to compute the vortex circulation [12]. With an empirical method derived from delta wing experiments, the peak-to-peak velocity difference at the assumed core radius is taken.

$$\Gamma = \frac{\pi}{1.2763}\Delta w_V 2r_c \qquad (7)$$

Again, the velocities and assumed core radii were taken from data in the wind tunnel system instead of the vortex axis system. In [4], all vortex circulations were computed using Eq. 7.

In Fig. 5 the vorticity distribution around the vortex of case BL, advancing side, is shown in the vortex coordinate system with using the original LDV data (a) and after data smoothing with an algorithm described in [33] (b). This data smoothing cuts the point-to-point scatter and therewith the peak values (and the integral value of circulation, too) but gives a clearer figure of where vorticity is concentrated and where the vortex center is located. It is clearly visible that there is no typical vortex present with a concentrated, almost symmetrical vorticity in the core. This is due to the interaction with the blade that just passed this vortex very closely and the wake of this blade is interacting with this vortex such that it is stretched to a flat band of vorticity. This wake is located directly below the lower border of the graph. Since one part of the vortex is above the top of the experimental data field, and another part of the vortex apparently mixed with the wake on the lower left of the figure, not all vorticity of the vortex could be included in the computation of circulation.

The MN case (advancing side, given in Fig. 6) does not show any vortex structure in the entire area of measurement, here given in the original wind tunnel coordinate system. Wakes of the last two blades that passed this area are visible, and it is to be assumed that the vortex, that must even have been stronger than that of the BL case (see Fig. 1, Tab. 3) passed either before the measurement time window was opened, or on a lower flight path such that it could not be captured. This latter assumption is more probable with the information of LLS data, Fig. 3, where the vortex appears to pass close to the lower end of the LDV range, and free-wake computations indicate both reasons to be true [29].

In the MV case, Fig. 7, two vortices are present as expected from Fig. 1. The lower vortex is spread over a larger area than the upper vortex and has lower absolute values in vorticity, but the integrated circulation is larger. Since two well separated centers of vorticity are present in the lower vortex, it either has been cut by a blade just before the LDV measurement has been taken, or the roll-up procedure resulted in this type of vortex structure. From Fig. 2 and Fig. 3 the vortex shall have passed high enough above the blades before the LDV measurement, and from Fig. 6 the blade wake has a strong vorticity, that cannot be found in Fig. 7. In contrast to this, the upper vortex has a center clearly to identify.

On the retreating side, the vortices are stronger at the time of creation than those of the advancind side and thus shall be more clearly to be identified from the LDV data. In the BL case, shown in Fig. 8, the vortex appears as a well-rounded structure with very large vorticity in the center. In the MN case, the vortex has much weaker vorticity and is spread over a larger area. This is most probably due to the fact that the vortex has had a very close interaction with a blade at $\psi = 280°$, a result from the blade's leading edge pressure distribution, see Fig. 2. In the MV case, the vortex again appears as a very round-shaped structure with large values of vorticity and a clear center.

The computed values of circulation are summarized in Tab. 5. It must be noted, that LDV data are always time averaged data and that the natural fluctuations in vortex position from revolution to revolution smooth the peak values to a certain degree, compared to in-

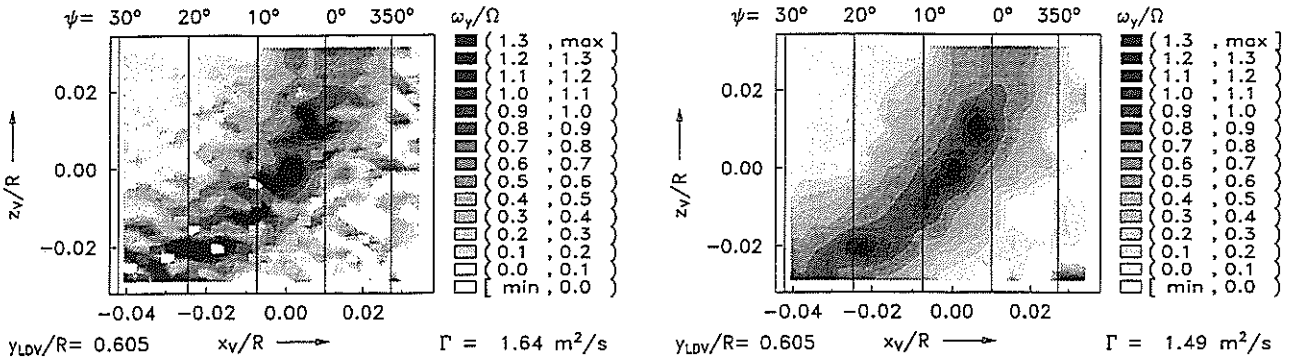

(a) original data

(b) smoothed data

Figure 5: Vorticity and vortex circulation, case BL, advancing side.

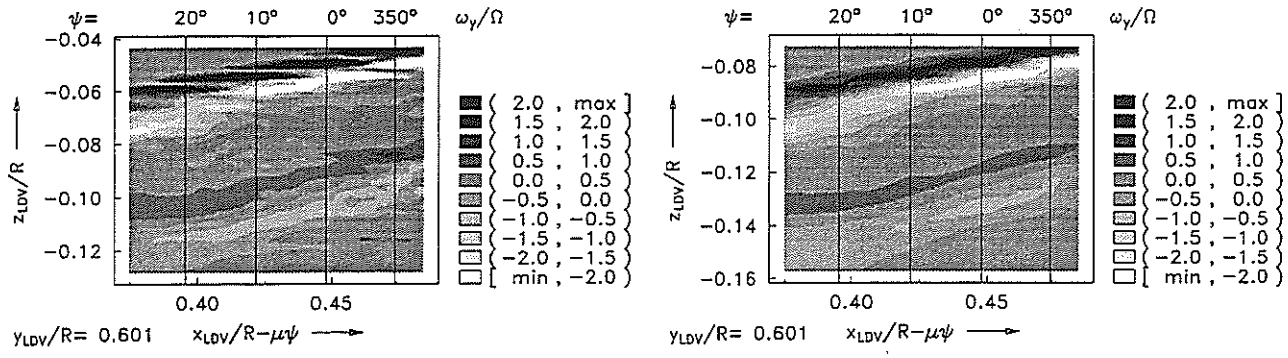

(a) original data

(b) smoothed data

Figure 6: Vorticity, case MN, advancing side.

Side	advancing			retreating		
Case	BL	MV	MV (u)	BL	MN	MV
$\frac{\Gamma_V^{(1)}}{m^2/s}$	2.65	3.73	-2.44	3.67	4.18	4.58
$\frac{\Gamma}{m^2/s}$	1.64	2.14	-1.53	2.50	1.73	3.46
$\frac{\Gamma^{(2)}}{m^2/s}$	2.13	2.78	-1.99	3.25	2.25	4.50
	from [31]			from [12]		
$\frac{\Gamma}{m^2/s}$	1.0	1.3	-1.0	2.1	2.2	2.8
	from [4]					
$\frac{\Gamma}{m^2/s}$	1.4	2.2	-1.6			

Table 5: Vortex circulation. (u) denotes the upper vortex. (1): Circulation trailed into the vortex at its generation from Tab. 3; (2): values of Γ multiplied by the empirical factor of 1.3 from [32].

stantaneous field measurements. A direct comparison between LDV data and PIV data on rotor vortices has been made in [32], and it was found that the circulation derived from the instantaneous field measurement was 1.3 the value of the LDV measurement field. As a first guess, this factor may be used to correct the LDV-based circulations. These values are also given in Tab. 5. With this correction, the vortex circulation from flow field data are getting close to the circulation initially trailed into the wake, Γ_V, derived in a section above. This is especially true for the vortex on the retreating side, MV case, where the leading edge pressure distribution of Fig. 2 predicted no interaction with a blade before reaching the LDV location. In the MN case, retreating side, a collision with a blade is visible before the vortex reaches the LDV location. The vorticity field in Fig. 8 shows a very diffuse distribution of vorticity, with a much lower value of circulation than in the other cases, although the inital vortex strength is predicted to be in between the BL and the MV case. The wake of the blade interacting with the vortex is within the vortex core and thus affects the integrated circulation.

Vortex core radii

In [4] the vortex cores are identified from velocity pro-

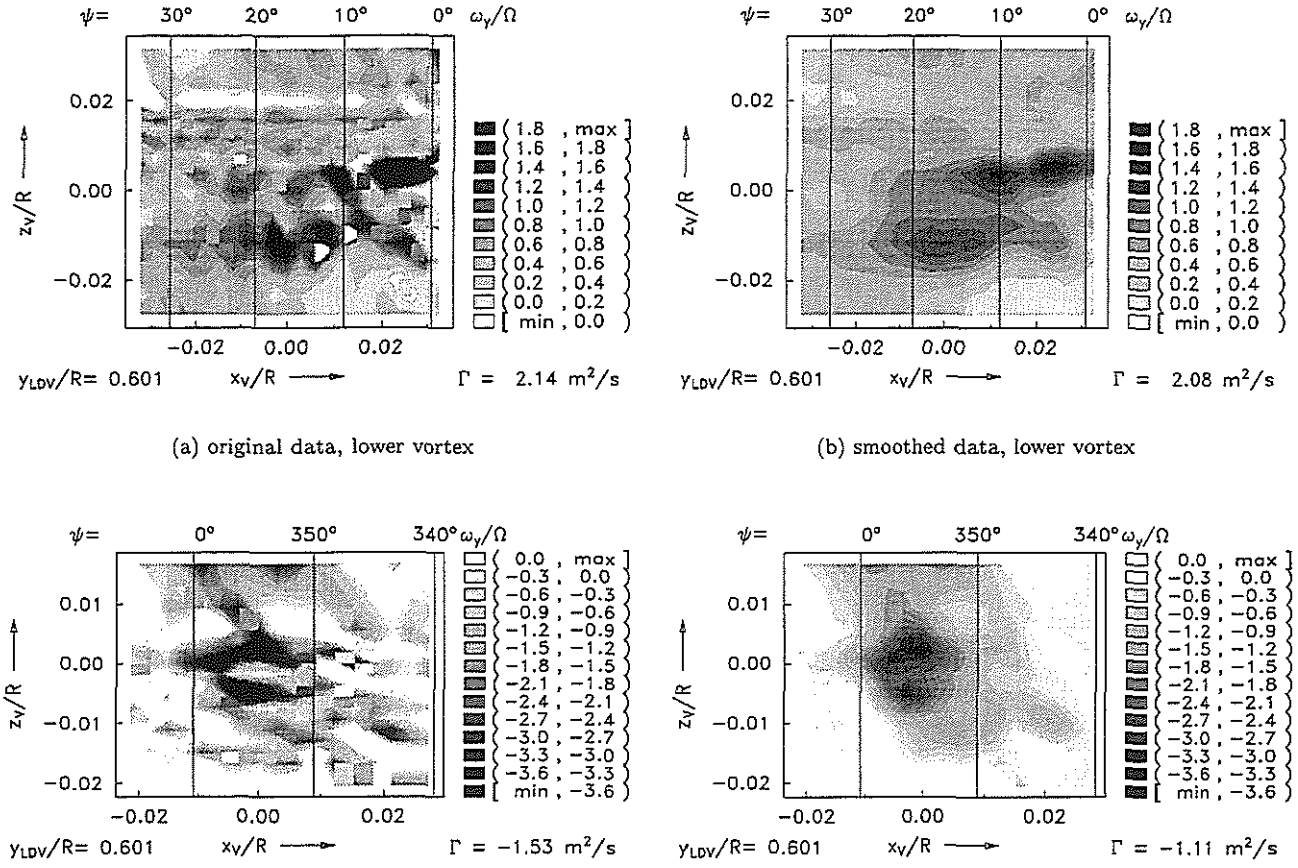

(a) original data, lower vortex

(b) smoothed data, lower vortex

(c) original data, upper vortex

(d) smoothed data, upper vortex

Figure 7: Vorticity and vortex circulation, case MV, advancing side.

files through the vortex core. Two possibilities for such an analysis are available, either from w versus x or from u versus z. In [4], both methods are used with the velocity profiles in the wind tunnel system, and the smaller value of both has been taken; mostly from the profile $u(z)$. Due to the vortex axis inclination given in Tab. 4, the vortex core radius in the vortex axis system will be significantly smaller. In Fig. 9 and Fig. 10 all velocity profiles $w(x)$ and $u(z)$ are given for the vortices found on the advancing side and on the retreating side, respectively, for cases BL, MN and MV. On the advancing side, no vortex is present in the MN case, but a counterrotating double vortex system in the MV case as shown in Fig. 7.

Since the velocity profiles of both the wind tunnel system and the vortex axis system are given, the differences are immediately visible. Due to large inclination angles β_z (see Tab. 4) the difference between the core radii from $w(x_{LDV})$ and those from $w_V(x_V)$ are larger than the differences in the appropriate $u(z)$-profiles. In most cases the peak-to-peak velocity difference is larger in the vortex axis system and the velocity profile is more pronounced. From the figures, the vortex core radii can be extracted, but care must be taken, where the wake of a blade is within the vortex core. This is mainly visible in the following $u(z)$ profiles: BL and MV on the advancing side and MN on the retreating side. In the other cases, the blade's wake is far enough outside the core such that the velocity profile is almost unaffected. Nevertheless the scatter of velocity data at the core radius has to be smoothed by hand to identify the location of peak velocity and thus the core radius. The vortex core radii evaluated this way are listed in Tab. 6 and extracted from Fig. 9 and Fig. 10. Also, they are empirically corrected by the results of [32], where the instantaneous flow field analysis by PIV technique directly was compared to LDV results of the same area, and the core radii were found to be 0.8 the size of those analysed by LDV. It must be noted, that in [4] the x-coordinate is constructed with the average velocity u_{av} within the entire LDV data field, not with usage of the wind tunnel speed μ as is done here. Thus small differences in the core radii derived from the wind tunnel system velocity profiles are present. In [4], most of the core radii are taken from the $u(z)$ profile, because they are smaller than those of the $w(x)$ profiles. From Tab. 6, the core radii from both of the velocity profiles are close together when analysed from the profiles in the vortex system. The differences to the values in the tunnel

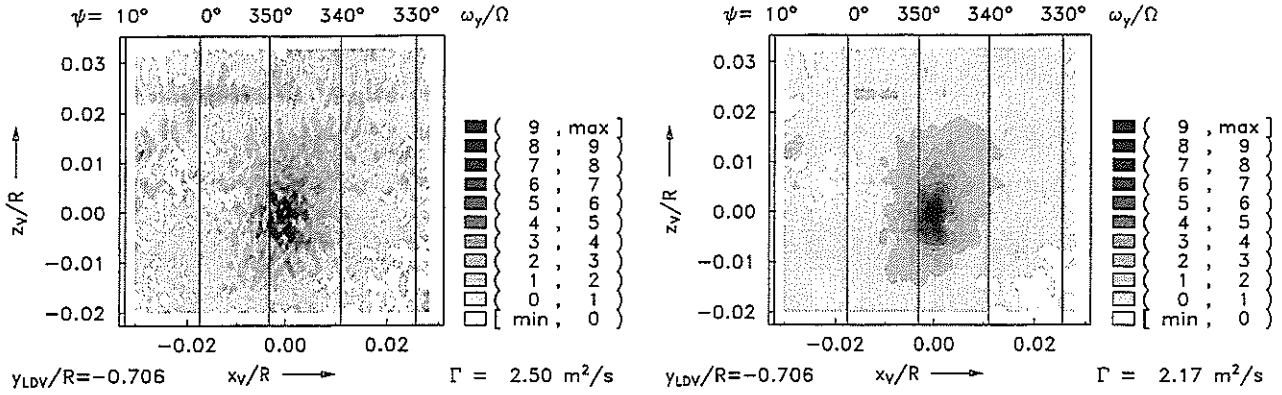

(a) original data, BL case

(b) smoothed data, BL case

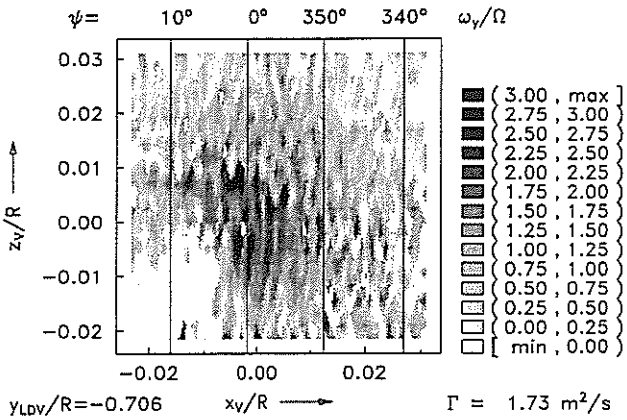

(c) original data, MN case

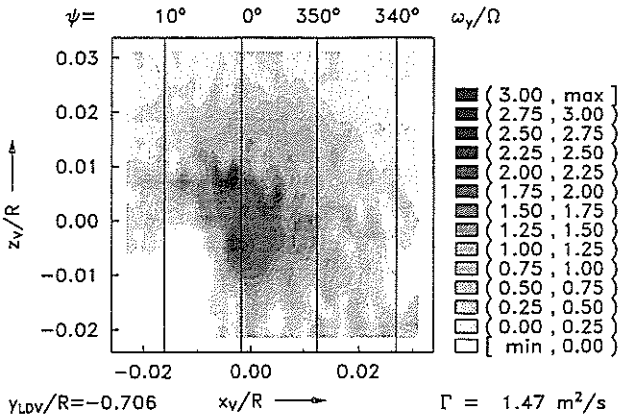

(d) smoothed data, MN case

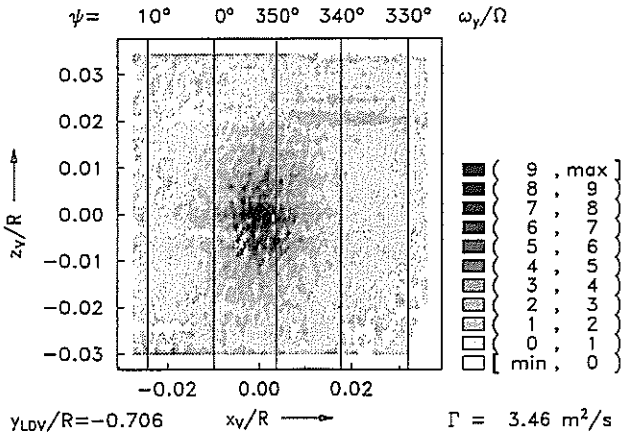

(e) original data, MV case

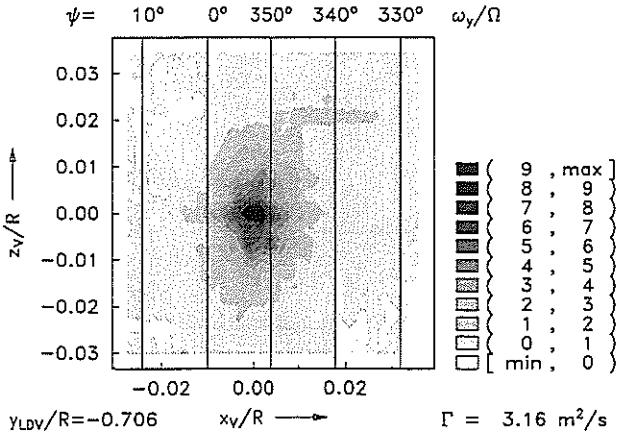

(f) smoothed data, MV case

Figure 8: Vorticity and vortex circulation, retreating side.

system are larger in the $w(x)$ profiles, because the inclination angle β_z has larger values than β_x, see Tab. 4.

Vortex axial velocities

In vortices created by a constant value of circulation (a wing in level flight) as well as in vortices created by dynamic changes of circulation (typically in rotorcraft) axial velocities exist from a theoretical standpoint [34] and have been measured by LDV on single and two-bladed untwisted rotors with small tip speed

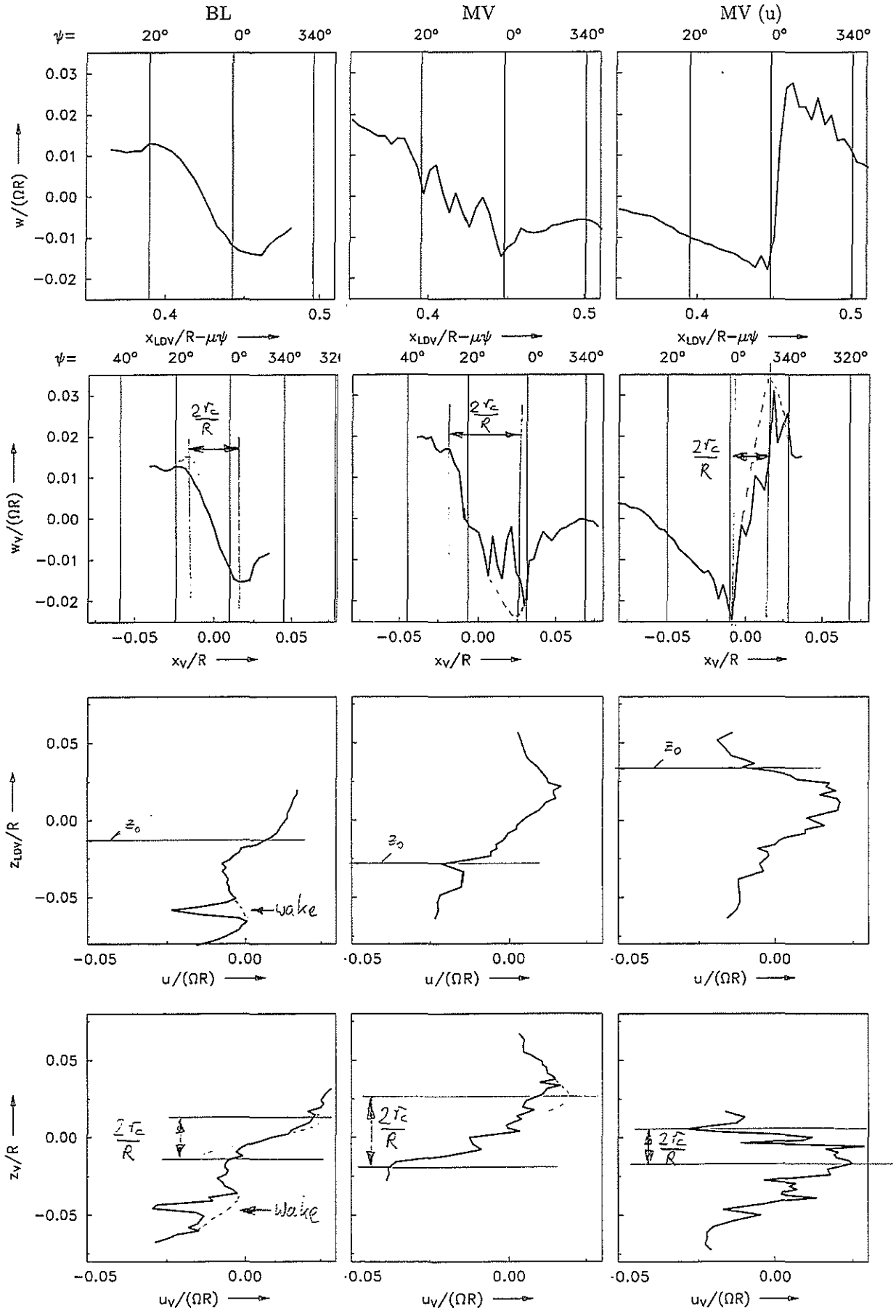

Figure 9: Velocity profiles through the vortex core (advancing side). Peak velocities mark the vortex core radius.

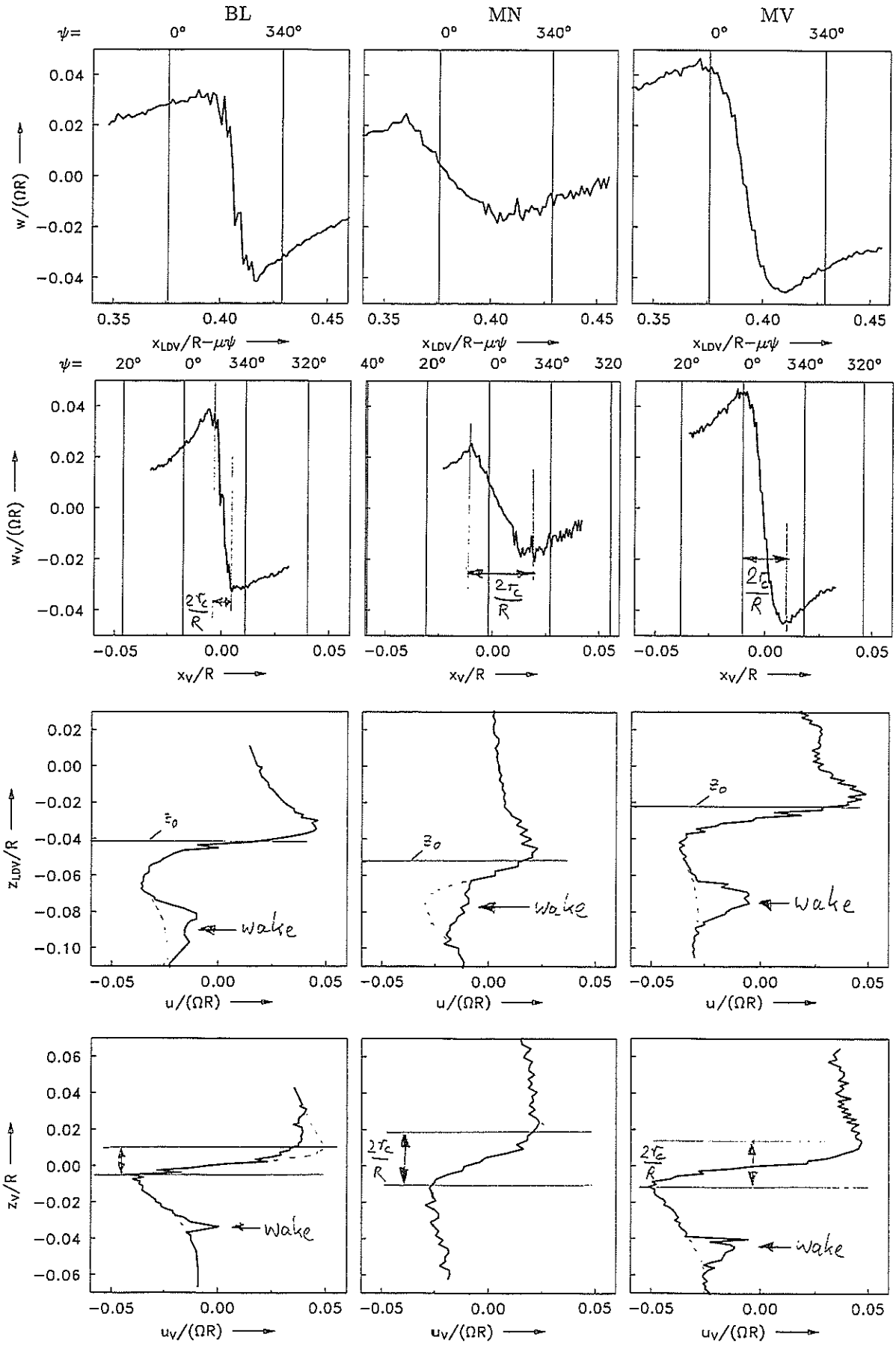

Figure 10: Velocity profiles through the vortex core (retreating side). Peak velocities mark the vortex core radius.

Side:	advancing						retreating					
Case:	BL		MV		MV (u)		BL		MN		MV	
System:	t	v	t	v	t	v	t	v	t	v	t	v
$w(x)$	2.3	1.5	3.7	2.3	1.7	1.1	1.0	0.7	2.5	1.5	1.9	1.0
$u(z)$	2.1	1.4	2.7	2.3	1.6	1.1	1.5	0.7	1.6	1.5	1.5	1.2
From [4]	2.1		2.7		1.6		1.5		2.5		1.5	
$80r_c/R^{(1)}$		1.1		1.8		0.9		0.6		1.2		0.8

Table 6: Vortex core radii $100\,r_c/R$ identified from velocity profiles of Fig. 9 and Fig. 10. (u) denotes the upper vortex, t=tunnel system, v=vortex axis system. $^{(1)}$ empirically corrected by the results from [32].

in [36]. It was found that the axial velocity quickly decreased with vortex age, and were negligible at wake ages larger than 90°. In [10], vortices of a four bladed model rotor with reduced tip speed were measured by LDV, and the peak axial velocity was found to be $v_V/(\Omega R) = 0.04$ for a rectangular blade at a vortex age of 40°, and -0.12 for a winglet blade. The first value agreed with earlier experiments [35].

The vortices measured in the HART test were little older than one revolution, and the rotor was operated at full scale Mach numbers. For the cases investigated here, the $v_V(x_V)$ velocity profiles through the vortex centers provide information about the shape and magnitude of axial velocities. The rate of change with time could not be measured with the experimental set-up of HART, but this is an important parameter for the vortex' stability. In Fig. 11 all axial velocity profiles are given. On the advancing side, only the upper vortex of the MV case has a significant axial flow within the vortex center, while the lower vortex and the vortex of case BL do only have small axial velocities. On the retreating side, all three cases show a clear axial velocity profile, only the magnitude is smaller in the MN case, because this vortex was cut by a blade before as can be seen in Fig. 2, Fig. 8 and Fig. 10. Compared to the outer flow, the axial velocity peaks at $v_V/(\Omega R) = 0.064$, and thus is even larger than the circumferential velocities u_V and w_V of Fig. 9 and Fig. 10. For a Rankine type of vortex (solid core with constant vorticity, no vorticity outside the core) a formula is given in [34] for the axial velocity distribution inside and outside the core. For an observer moving with the vortex, outside the core $v_V = 0$, and inside the core $r < r_c$:

$$v_V(r) = \sqrt{V_\infty^2 + 2\omega_y^2(r_c^2 - r^2)} - V_\infty \qquad (8)$$

In a rotor environment, $V_\infty = \Omega R(r_t/R + \mu \sin\psi_t)$ is the velocity at the radius and the time of tip vortex creation, and the constant value of vorticity may be replaced by the circulation with $\omega_y = \Gamma/(2\pi r_c^2)$ (from Eq. 5). The peak value appears in the center of the vortex at $r = 0$. With the values of r_t/R from Tab. 3, ψ_t from Fig. 1, Γ from Tab. 5 and r_c/R from Tab. 6, the peak values can be approximated theoretically. In Tab. 7 both the theoretical and the experimental peak values of axial velocity are compared. A third row of data is computed using the empirical correction factors found in [32] for the vortex circulation (1.3) and its core radius (0.8). In general, agreement with the experimental data is poor, when the vortices are not concentrated, and thus cannot be approximated by the type of vortex used in theory (all vortices on the advancing side, MN on the retreating side). The vortices not affected by BVI before being measured by LDV, that are BL and MV on the retreating side, show fair agreement when the empirically corrected circulation and core radius are used in Eq. 8.

Vortex passage through the LDV range

In Fig. 9 and Fig. 10 the vertical height of the vortex' center passing the LDV measurement range can be extracted from the $w(x)$ and $u(z)$ profiles, respectively. The center of the vortex was chosen from the vorticity plots in Fig. 5, Fig. 7 and Fig. 8, from the axial velocity distribution in the vortex coordinate system and from the velocity vector plot (both not given here). Due to the crossflow component of velocity, the vortex center coordinates x_0/R or ψ_0 and z_0/R, also given in $w(x)$ and $u(z)$ profiles, seem not always to be in the vortex center, but the $w_V(x_V)$ and $u_V(z_V)$ profiles indicate the correct position with the coordinate origin in the center of the velocity profile, especially at the retreating side (Fig. 10). In addition, the time of passage in terms of rotor azimuth, ψ_0, can be extracted by

$$\psi_0 = \frac{x_{LDV}/R - x_0}{\mu} \qquad (9)$$

In Tab. 8 these values are listed and compared to what has been analysed from LLS data some sections before, see Tab. 4. There are significant differences between the results of the two methods of up to $\Delta z_0/R = 0.026$ (that is almost half a chord) in vertical position and $|\Delta\psi_0| = 30°$ ($\equiv |\Delta x/R| = 0.079$, that are 1.3 chords) and it is unclear where these discrepancies do come from. Interestingly the BL case is the only one with opposite sign in both of the differences compared to the other cases. The LLS results are expected to have an accuracy of $10mm$ in vortex positions ($\equiv \Delta z/R = 0.005$) and the LDV positions are accurate to about $1mm$ in LDV position, and 0.5° in azimuth; all of these values are well below the discrepancies found. It must be noted, that the vortex passage height and time using LLS data is an interpolation on the retreating side (Fig. 4), and shall be more reliable than on the advancing side, where the vortex flight path is extrapolated

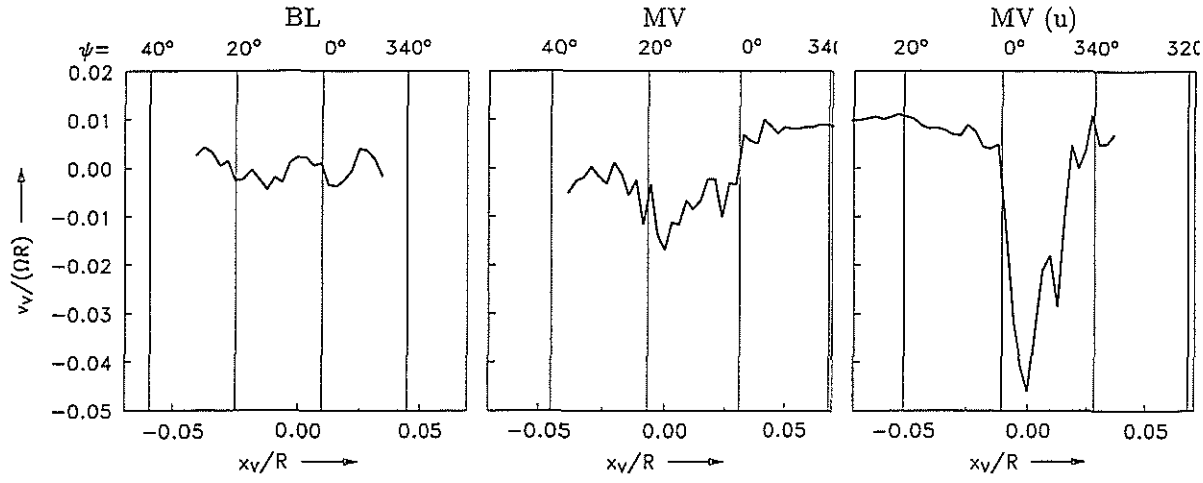

(a) advancing side

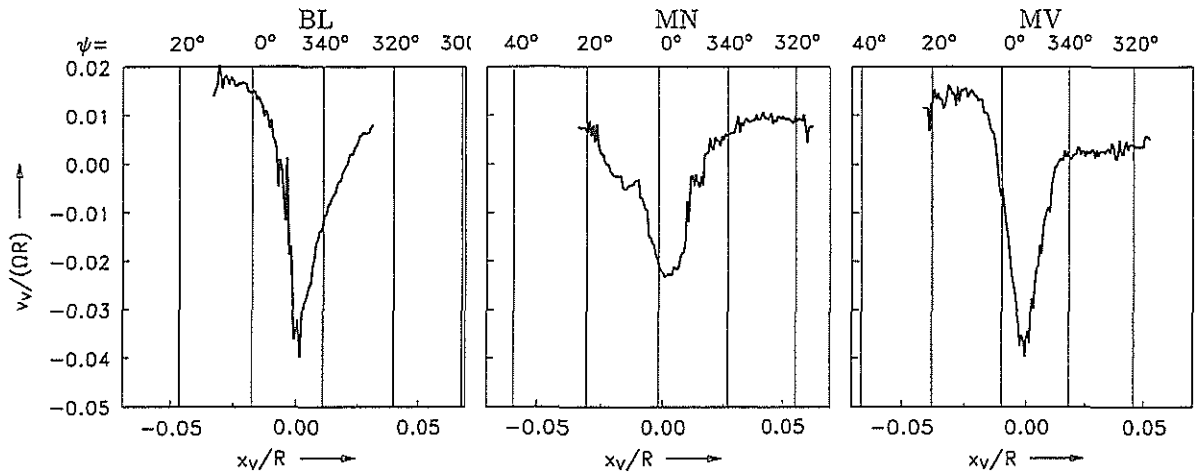

(b) retreating side

Figure 11: Axial velocity profiles.

Side:	advancing			retreating		
Case:	BL	MV	MV (u)	BL	MN	MV
$\psi_V/(2\pi)$	1.35	1.12	1.35	1.12	1.12	1.12
$100v_V/(\Omega R)^{(1)}$	0.7	1.9	5.6	6.4	3.3	4.7
$100v_V/(\Omega R)^{(2)}$	0.2	0.1	0.3	2.2	0.2	1.7
$100v_V/(\Omega R)^{(3)}$	0.5	0.3	0.8	5.7	0.6	4.4

Table 7: Vortex age and maximum axial velocities in the vortex center. $^{(1)}$: Experiment; $^{(2)}$: Eq. 8 with Γ from Tab. 5 and r_c from Tab. 6; $^{(3)}$: as $^{(2)}$ using empirically corrected core radii and circulation from [32].

(Fig. 3). In average, LLS predicts the vortices to be $\Delta z_0/R = 0.022$ higher, or $0.36c$, a small value compared to the rotor radius, but a large value compared to vortex core radii dimensions.

The difference in coordinates of the vortex passage at the LDV location obtained by the different techniques of LLS and LDV have to be analysed. The LDV systems are erected outside of the tunnel flow on towers on the right and left of the test section. They are directing into the flow at an angle of 90° from aside with a measurement distance of $5m$. Since the towers are outside the flow, they are only subject to thermal effects, and might deform vertically due to heating. This might explain part of the differences in vertical direction, $\Delta z_0/R$, but not the differences in time, $\Delta\psi_0$, since both LLS and LDV are triggered to the rotor azimuth.

The LLS camera is mounted on the nozzle exit, $3.6R$ ahead and $1.5R$ above the rotor hub. The areas of interest are located between $0.35R$ and $0.8R$ behind the hub on the advancing side and between $0.15R$ and $0.6R$ behind the hub on the retreating side. In average, the horizontal LLS measurement distance is about $4.1R$ and the total distance $4.37R$. Thus, the measurement angle is about $\alpha = 20°$ downwards. Any angular deflection $\Delta\alpha$ of the camera, be it elastic deformation of the nozzle, or thermal deformation, will cause an error in hor-

Side:	advancing			retreating		
Case:	BL	MV	MV (u)	BL	MN	MV
$100z_0/R$	-1.3	-2.8	3.4	-4.1	-5.3	-2.3
$100\Delta z_0/R^{(1)} = 100(z_0\|_{LLS} - z_0\|_{LDV})/R$	-1.0	2.4	2.6	2.3	1.3	2.3
$\psi_0/^o$	6	16	355	348	359	353
$\Delta\psi_0/^{o\ (1)} = (\psi_0\|_{LLS} - \psi_0\|_{LDV})/^o$	24	-24	-15	-22	-30	-29

Table 8: Vortex height z_0 and time ψ_0 of passage through the LDV measurement range. (u) denotes the upper vortex. $^{(1)}$: Δ values are the difference to the results of LLS data, see Fig. 3, Fig. 4, and Tab. 4.

izontal and vertical position of the LLS camera frame. The average vertical difference found between both of the methods is $\Delta z_0/R = 0.022$, and this amounts for an angular difference of $\Delta\alpha = 0.27^o$ at the camera location. The horizontal difference then becomes

$$\Delta\psi_0 \approx \Delta z_0/(R\mu\sin\alpha) = 24^o \qquad (10)$$

This is just the range found in Tab. 8. However, further investigations have to be done to prove this assumption.

Conclusions

In this paper pressure data, LLS data and LDV data of the HART test are investigated in detail in order to extract vortex characteristics and to assess the consistency of data from different measurement techniques. The conclusions can be summarized as:

- The vortex core radii evaluated from data in the vortex axis system are generally smaller than those from data in the wind tunnel system, the smallest core is found to be only $r_c/R = 0.007$, i.e. 12% of the chord at a vortex age of slightly more than one revolution.
- Within the vortex core, an axial velocity exists, that is very large in vortices that have not been under BVI before. In these vortices, vorticity is very concentrated in the center, and the cores are small.
- Where BVI already affected the vortex, its strength is decreased, the core is widened, and vorticity is spread over a wider area. The axial velocity is reduced.
- It is found that the height of the vortex passage identified from LLS and from LDV data are not consistent. LLS data indicate the vortex in all cases to fly higher than the vertical position found in the LDV data. The differences range from $\Delta z/R = 0.014$ to 0.03 with an average of $\Delta z/R = 0.023$.
- It is also found, that the time of the vortex passage identified from LLS and from LDV data are not consistent. In terms of rotor azimuth, the differences range from $\Delta\psi = 32^o$ on the advancing side to -30^o on the retreating side.
- The differences in LLS and LDV results may be due to small angular deflections of the LLS camera location, but this assumption has still to be investigated.
- Future measurements of rotor wakes shall be based on instantaneous flow field measurements and must be able to scan an entire area at the same instance of time to avoid the uncertainties of time averaging and vortex fluctuations. They shall cover a wider range of the rotor disk to provide information of the global structure, the vortex flight path, and the vortex aging process.

As a consequence of the investigations of this paper, the vortex properties like core radius and circulation assumed before, have to be corrected. This is due to the fact that earlier investigations analysed the LDV data in the wind tunnel coordinate system and did not take into account the vortex orientation in space. A second consequence derives from the result, that inconsistencies of data from LLS and LDV technique were found and the reasons have to be analysed in future.

References

[1] W.R. Splettstößer, G. Lehmann, B.G. van der Wall, *Higher Harmonic Control of a Helicopter Model Rotor to reduce Blade/Vortex Interaction Noise,* Z. Flugwiss. Weltraumforschung 14, p. 109-116, Springer Verlag, 1990

[2] Y.H. Yu, B. Gmelin, H. Heller, J.J. Philippe, E. Mercker, J.S. Preisser, *HHC Aeroacoustic Rotor Test at the DNW - The Joint German/French/US HART Project* -, 20^{th} European Rotorcraft Forum, Amsterdam, Netherlands, 1994

[3] B. Gmelin, H. Heller, E. Mercker, J.J. Philippe, J.S. Preisser, Y.H. Yu, *The HART Programme - a Quadrilateral Cooperative Research Effort,* 51^{st} Annual Forum of the American Helicopter Society, Fort Worth, TX, USA, 1995

[4] W.R. Splettstößer, R. Kube, U. Seelhorst, W. Wagner, A. Boutier, F. Micheli, *Higher Harmonic Control Aeroacoustic Rotor Test (HART) - Test Documentation and Representative Results* -, DLR IB 129-95/28, Braunschweig, Germany, 1995

[5] W.R. Splettstößer, K.J. Schultz, B. Junker, W. Wagner, B. Weitemeier, *The HELINOISE Aeroacoustic Rotor Test in the DNW,* DLR-Mitt. 93-09, Braunschweig, Germany, 1993

[6] B. Gelhaar, B. Junker, W. Wagner, *DLR - Rotor Teststand Measures Unsteady Rotor Aerodynamic Data,* 19^{th} European Rotorcraft Forum, Como, Italy, 1993

[7] R.M. Martin, W.R. Splettstößer, K.J. Schultz, J.W. Elliot, *Acoustic Measurements from a Rotor Blade-Vortex Interaction Noise Experiment in the German-Dutch Wind Tunnel (DNW),* NASA TM-4024, AVSCOM TR 87-B-4, 1988

[8] E. Mercker, K. Pengel, *Flow Visualization of Helicopter Blade-Tip Vortices - a qualitative Technique to Determine the Trajectory and the Position of the Tip Vortex Pattern of a Model Rotor,* 18^{th} European Rotorcraft Forum, Avignon, France, 1992

[9] U. Seelhorst, K.A. Bütefisch, K.H. Sauerland, *Three Component Laser-Doppler Velocimeter Development for Large Wind Tunnel,* ICIASF '93 Record, pp.33.1-33.7, 1993

[10] U. Seelhorst, *Untersuchung von Rotorblattspitzenwirbeln mittels eines 3 Komponenten Laser-Doppler Anemometers,* DLR FB 96-15, 1996

[11] A. Boutier, J. Lefèvre, D. Soulevant, F. Dunand, *2D Laser Velocimetry near Helicopter Blades in DNW (NLR),* ICIASF '93 Record, pp.32.1-32.8, 1993

[12] A. Boutier, J. Lefèvre, F. Micheli, *3D Laser Velocimetry and Blade Tip Attitude Measurements by TART Method within the HART Test Program,* ONERA RTS 5/51432 PY, Chatillon, France, 1996

[13] Y.H. Yu, C. Tung, J.M. Gallman, W.R. Splettstößer, K.J. Schultz, B.G. van der Wall, P. Spiegel, G. Rahier, B. Michéa, M. Costes, *Aerodynamics and Acoustics of Rotor Blade-Vortex Interactions: Analysis Capability and its Validation,* AIAA 93-4332, 15^{th} AIAA Aeroacoustics Conference, Long Beach, CA, USA, 1993

[14] P. Beaumier, J. Prieur, G. Rahier, P. Spiegel, A. Demargne, C. Tung, J.M. Gallman, Y.H. Yu, R. Kube, B.G. van der Wall, K.J. Schultz, W.R. Splettstößer, T.F. Brooks, C.L. Burley, D.D. Boyd, Jr., *Aerodynamic and Acoustic Effects of Higher Harmonic Control on Helicopter rotor Blade-Vortex Interaction: Predictions and Preliminary Validation,* 75^{th} AGARD Fluid Dynamics Panel Meeting and Symposium on Aerodynamics and Acoustics of Rotorcraft, Berlin, Germany, 1994

[15] R. Kube, B.G. van der Wall, K.J. Schultz, *Mechanisms of Vibration and BVI Noise Reduction by Higher Harmonic Control,* 20^{th} European Rotorcraft Forum, Amsterdam, Netherlands, 1994

[16] Y.H. Yu, C. Tung, J.M. Gallman, K.J. Schultz, B.G. van der Wall, P. Spiegel, B. Michéa, *Aerodynamics and Acoustics of Rotor Blade-Vortex Interactions,* Journal of Aircraft, Vol. 32, No. 5, 1995

[17] R. Kube, W.R. Splettstößer, W. Wagner, U. Seelhorst, Y.H. Yu, A. Boutier, E. Mercker, *Initial Results from the Higher Harmonic Aeroacoustic Rotor Test (HART) in the German-Dutch Wind Tunnel,* 75^{th} AGARD Fluid Dynamics Panel Meeting and Symposium on Aerodynamics and Acoustics of Rotorcraft, Berlin, Germany, 1994

[18] J.M. Gallman, C. Tung, K.J. Schultz, W.R. Splettstößer, H. Buchholz, P. Spiegel, C.L. Burley, T.F. Brooks, D.D. Boyd, Jr., *Effect of Wake Structure on Blade-Vortex Interaction Phenomena: Acoustic Prediction and Validation,* 1^{st} Joint CEAS/AIAA Aeroacoustics Conference, Munich, Germany, 1995

[19] W.R. Splettstößer, R. Kube, U. Seelhorst, W. Wagner, A. Boutier, F. Micheli, E. Mercker, K. Pengel, *Key Results from a Higher Harmonic Control Aeroacoustic Rotor Test (HART) in the German-Dutch Wind Tunnel,* 21^{st} European Rotorcraft Forum, Saint-Petersburg, Russia, 1995

[20] E. Mercker, K. Pengel, R. Kube, B.G. van der Wall, A. Boutier, F. Micheli, *On the Blade Deformation Measured at a Scaled Helicopter Rotor,* 2^{nd} International Aeromechanics Specialists' Conference, Bridgeport, CT, USA, 1995

[21] C. Tung, J.M. Gallman, R. Kube, W. Wagner, B.G. van der Wall, T.F. Brooks, C.L. Burley, D.D. Boyd, Jr., G. Rahier, P. Beaumier, *Prediction and Measurement of Blade-Vortex Interaction Loading,* 1^{st} Joint CEAS/AIAA Aeroacoustics Conference, Munich, Germany, 1995

[22] P. Beaumier, P. Spiegel, *Validation of ONERA Prediction Methods for Blade-Vortex Interaction using HART Results,* 51^{st} Annual Forum of the American Helicopter Society, Fort Worth, TX, USA, 1995

[23] K. Ehrenfried, W. Geißler, U. Seelhorst, H. Vollmers, *Combined Numerical and Experimental Investigations of BVI-Noise Generation and Radiation from the HART-Test Campaign,* 21^{st} European Rotorcraft Forum, Saint-Petersburg, Russia, 1995

[24] N. Jobard, M. Costes, P. Beaumier, *Three Dimensional BVI Simulation on Aeroelastic Blades Using a New Deforming Grid Approach Coupled to a*

Free-Wake Analysis, 52^{nd} Annual Forum of the American Helicopter Society, Washington, DC, USA, 1996

[25] Y.H. Yu, C. Tung, S. Low, *Blade Aeroelastic Effect on Rotor Blade-Vortex Interaction (BVI) Noise,* 52^{nd} Annual Forum of the American Helicopter Society, Washington, DC, USA, 1996

[26] Y.H. Yu, *Rotor Blade-Vortex Interaction Noise: Generating Mechansms and its Control Concepts,* American Helicopter Society Specialist Meeting on Aeromechanics Technology and Product Design for 21^{st} Century, Bridgeport, CT, 1995

[27] T.F. Brooks, D.D. Boyd, Jr., C.L. Burley, J.R. Jolly, Jr., *Aeroacoustic Codes For Rotor Harmonic and BVI Noise - CAMRAD.Mod1/HIRES,* 2^{nd} AIAA/CEAS Aeroacoustics Conference, State College, PA, USA, 1996

[28] R. Kube, W.R. Splettstößer, W. Wagner, U. Seelhorst, Y.H. Yu, C. Tung, P. Beaumier, J. Prieur, G. Rahier, P. Spiegel, A. Boutier, T.F. Brooks, C.L. Burley, D.D. Boyd, Jr., E. Mercker, K. Pengel, *HHC Aeroacoustic Rotor Tests in the German Dutch Wind Tunnel: Improving Physical Understanding and Prediction Codes,* 52^{nd} Annual Forum of the American Helicopter Society, Washington, DC, USA, 1996

[29] B.G. van der Wall, *Free-Wake Analysis on Massively Parallel Computers and Validation with HART Test Data,* 53^{rd} Annual Forum of the American Helicopter Society, Virginia Beach, VA, USA, 1997

[30] E. Mercker, *Compilation of Test Data for the HART-Test,* DNW-TR-94.03, DNW Emmeloord, Netherlands, 1994

[31] U. Seelhorst, K.H. Sauerland, F. Schmidt, H. Vollmers, K.A. Bütefisch, W. Geißler, *3D Laser-Doppler-Velocimeter Measurements within the HART-Test Program,* DLR IB 223 94 A 37, Göttingen, Germany, 1995

[32] M. Raffel, U. Seelhorst, C. Willert, H. Vollmers, K.A. Bütefisch, J. Kompenhans, *Measurement of Vortical Structures on a Helicopter Rotor Model in a Wind Tunnel by LDV and PIV,* 8^{th} International Symposium on Applications of Laser Techniques to Fluid Mechanics, Lisbon, 1996

[33] *TECPLOT Version 6, User's Manual,* Amtec Engineering, Inc., USA, 1994

[34] G.K. Batchelor, *Axial Flow in Trailing Line Vortices,* Journal of Fluid Mechanics, Vol. 20, 1964

[35] K.L. Orloff, *Trailing Vortex Wind-Tunnel Diagnostics with a Laser Velocimeter,* J. Aircraft, Vol. 11, No. 8, pp. 477-482, 1974

[36] A.J. Coyne, M.J. Bhagwat, J.G. Leishman, *Investigation into the Rollup and Diffusion of Rotor Tip Vortices using Laser Doppler Velocimetry,* 53^{rd} Annual Forum of the American Helicopter Society, Virginia Beach, VA, USA, 1997